minerals

MDPI

Article

Occurrence of SiC and Diamond Polytypes, Chromite and Uranophane in Breccia from Nickel Laterites (New Caledonia): Combined Analyses

Yassine El Mendili [1,2,*], Beate Orberger [3], Daniel Chateigner [1], Jean-François Bardeau [4], Stéphanie Gascoin [1], Sébastien Petit [1] and Olivier Perez [1]

[1] CRISMAT-ENSICAEN, UMR CNRS 6508, Université de Caen Normandie, IUT Caen, Normandie Université, 6 boulevard Maréchal Juin, 14050 Caen, France; daniel.chateigner@ensicaen.fr (D.C.); stephanie.gascoin@ensicaen.fr (S.G.); sebastien.petit@ensicaen.fr (S.P.); olivier.perez@ensicaen.fr (O.P.)
[2] Laboratoire ESITC Caen-COMUE Normandie Université, 1 Rue Pierre et Marie Curie, 14610 Epron, France
[3] GEOPS, Université Paris Saclay-Paris Sud, UMR 8148 (CNRS-UPS), Bât 504, 91405 Orsay, France; beate.orberger@universite-paris-saclay.fr
[4] IMMM, Le Mans Université, UMR6283 CNRS, Avenue Olivier Messiaen, 72085 Le Mans, France; jean-francois.bardeau@univ-lemans.fr
* Correspondence: yassine.el-mendili@esitc-caen.fr; Tel.: +33-231-452-628

Abstract: Different techniques have been combined to identify the structure and the chemical composition of siliceous breccia from a drill core of nickel laterites in New Caledonia (Tiebaghi mine). XRD analyses show quartz as a major phase. Micro-Raman spectroscopy confirmed the presence of reddish microcrystalline quartz as a major phase with inclusion of microparticles of iron oxides and oxyhydroxide. Lithoclasts present in breccia are composed of lizardite, chrysotile, forsterite, hedenbergite and saponite. The veins cutting through the breccia are filled with Ni-bearing talc. Furthermore, for the first time, we discovered the presence of diamond microcrystals accompanied by moissanite polytypes (SiC), chromite ($FeCr_2O_4$) and uranophane crystals ($Ca(UO_2)_2(SiO_3OH)_2.5(H_2O)$) and lonsdaleite (2H-[C-C]) in the porosities of the breccia. The origin of SiC and diamond polytypes are attributed to ultrahigh-pressure crystallization in the lower mantle. The SiC and diamond polytypes are inherited from serpentinized peridotites having experienced interaction with a boninitic melt. Serpentinization, then weathering of the peridotites into saprolite, did not affect the resistant SiC polytypes, diamond and lonsdaleite. During karstification and brecciation, silica rich aqueous solutions partly digested the saprolite. Again, the SiC polymorph represent stable relicts from this dissolution process being deposited in breccia pores. Uranophane is a neoformed phase having crystallized from the silica rich aqueous solutions. Our study highlights the need of combining chemical and mineralogical analytical technologies to acquire the most comprehensive information on samples, as well as the value of Raman spectroscopy in characterizing structural properties of porous materials.

Keywords: Ni-laterites; mineralogy; breccia; uranium; SiC; combined analyses; Raman

Citation: El Mendili, Y.; Orberger, B.; Chateigner, D.; Bardeau, J.-F.; Gascoin, S.; Petit, S.; Perez, O. Occurrence of SiC and Diamond Polytypes, Chromite and Uranophane in Breccia from Nickel Laterites (New Caledonia): Combined Analyses. *Minerals* **2022**, *12*, 196. https://doi.org/10.3390/min12020196

Academic Editors: Cristina Domènech and Cristina Villanova-de-Benavent

Received: 8 December 2021
Accepted: 28 January 2022
Published: 2 February 2022

1. Introduction

The occurrences of moissanite (SiC) associated with NiMnCo, FeSi and FeC alloys, are described from many peridotites and podiform chromitites belonging to ophiolites in Turkey, China, Myanmar, Russia, Mexico and Cuba [1–5]. Moissanite, natural SiC, is extremely rare. It was found in meteorite, kimberlites [6], metasomatic rocks [7], peridotites, serpentinites and podiform chromitites [8,9]. Moissanite intergrowth with other minerals have also been documented in eclogites and serpentinites from the Dabie-Sulu belt in China [9,10] and in volcanic rocks [7,11]. The more frequent natural moissanite are the 3C, 4H, 6H and 15R polytypes, where C, H and R polytypes are cubic, hexagonal, and rhombohedral, respectively. All these phases form at extremely low oxygen fugacity, 5 to 6

log units below the IW buffer [12]. The stability of these phases at surface conditions is explained by rapid tectonic uplift, while slow tectonic uplift would lead to diamond decomposition, as the observed graphitized diamonds from the Beni Bousera, Morocco [13] and the Ronda massifs, Spain [14]. Based on mineralogical studies, the super reduced association of moissanite, native Cu, Fe–Mn alloy in Al rich chromitite from the Mercedita ophiolite in Cuba was attributed to a low temperature serpentinization process in a very reduced microenvironment [4,15,16]. A similar model was proposed for micro diamonds found in chromite in podiform chromitite in serpentinite from the Tehuitzingo ophiolite in South Mexico [16].

None of these minerals and mineral association have been so far described from nickel laterite profiles. Recent studies by El Mendili et al. [17] give a detailed description of the 6O-SiC polytype in the siliceous breccia studied here. Its presence in an alteration profile is attributed to a three-stage process: formation in the lower mantle, transport into the upper mantle peridotite by second stage melts, weathering, and preservation in breccia pores.

Uranophane is a hydrous silicate ($Ca(UO_2)_2(SiO_3OH)_2.5(H_2O)$) occurring commonly as secondary minerals in oxidizing silica rich environment, fractures, mainly as result of uraninite (UO_2) alteration related to uranium and associated metal mineralization or nuclear fuel [18–20]. In laterites (Parana sedimentary basin, Brazil, hosting sedimentary and ultramafic-mafic intrusive rocks), uranophane was discovered in uraniferous nodules described from iron crusts [21]. Uraniferous minerals are not yet described from nickel laterites and New Caledonian rocks so far.

In this study, we report the first occurrence of diamond, lonsdaleite, moissanite among other reduced phases, and uranophane from silica rich rocks at the base of a nickel laterite profile, located in saprolite, at the Tiebaghi mine, New Caledonia. The silica rich rocks (sample ER-NC00-0001) was analyzed in the frame of the H2020 EU project SOLSA to evaluate the influence of surface roughness on close sensor drill core analyses [22,23].

2. Materials and Methods

2.1. Material

The siliceous dissolution breccia (SB; SOLSA label: ER-NC00-0001, Geographic coordinates: Latitude: 20°26′24.59″ S, Longitude: 164°13′1.20″ E) was sampled from a drill core performed in the nickel laterite profile at the Tiébaghi Mine in the northwestern part of New Caledonia.

2.2. Geological Setting

New Caledonia located in the Pacific Ocean 200 km off-shore NE Australia, represents a microcontinent composed of an autochtonous basement of metamorphic and metavolcanosedimentary rocks of Upper Carboniferous to Lower Cretaceous age, and Late Cretaceous to Lower Tertiary allochtonous terranes. Part of these terranes is the New Caledonia ophiolite [24–26]. The lower part of this ophiolite covers large terranes of the southern part of the island, while tectonic ophiolitic klippes occur in the northwestern part. The lithologies comprise serpentinized harzburgite (±lherzolite), and serpentinized pyroxenite, wherlite and dunite overlain by gabbro [25,26]. At Tiébaghi, the peridotites are much richer in chromite and show a higher diversity (dunites, harzburgite, lherzolite, pyroxenites), which may be related to magmatic differentiation and melt rock interactions [27]. Numerous dykes, sometimes pegmatitic, cut through the ultramafic rocks [28].

Lateritization of the ophiolite started in Oligocene (24 ± 5 Ma) [29] and resulted in the formation of world-class nickel laterite ore deposits in the lower part of the regolith. These nickel deposits represent ~9% of the world reserves [30]. Classically, the serpentinized peridotites decomposed into (a) sap-rock, representing serpentinized lithoclasts occurring in a soil matrix, (b) the nickel-rich saprolite, overlain successively by yellow and red laterite, with (c) a top layer of ferricrete. During lateritization, silicates (relict olivines and pyroxenes) are dissolved, and serpentines of several generations are gradually transformed into clay minerals and talc, while dissolved iron precipitates as oxy hydroxides and

dissolved silica as quartz [31]. Nickel is often enriched in the latest serpentine generation (3 wt.%) and talc-like phases such as kerolite (about a factor 10 richer than serpentines: 30 wt.% [23,32–34]. Meteoric alteration starting at 24 ± 5 Ma, is favored by an intense fracture network related to orogenic and post-orogenic (relaxation) tectonics [35–39]. In this high hydraulic conductivity environment, aquifers percolate at different levels of the laterite profile reserves [40] and form pseudo-karstic structures [36,41,42]. At Tiébhagi, the lower aquifer drains the fine and coarse saprolite and the highly fractured serpentinized peridotites [40,41]. Dissolution, and resorption of serpentinized peridotite related to down drainage meteoric water are observed [40]. This alteration caused the emplacement of a collapse breccia (>50% clasts) [41] along vertical channels and egg-shape morphologies at the base of the laterite profile related in particularly, the egg-shape morphology at the base of the saprolites, to alteration at hydrothermal temperatures (70–90 °C) [40,43]. Based on fluid flow modelling, the authors suggest that meteoric waters heated-up through exothermic reactions associated with serpentine weathering.

2.3. Sample Description

At Tiébaghi, the lower part of the regolith hosts a white-beige-brownish, porous silica rich rock. It has a typical boxwork structure (Figure 1). This rock hosts a few fragments, relicts of saprolite. It is a dissolution breccia. We call it hereafter siliceous breccia. The overall grain size of the breccia is <2 mm. The breccia is mainly composed of quartz of millimetric size, red spots represent iron oxyhydroxides, and locally black oxides occur (<1 mm). Crosscutting veins are filled with talc and clay minerals [22]. The studied samples were cut out from the drill core surfaces as prisms of ≈20 × 20 × 6 mm^3 size. From macroscopic observations, the formation of this breccia can be related to the epikarstic processes [40].

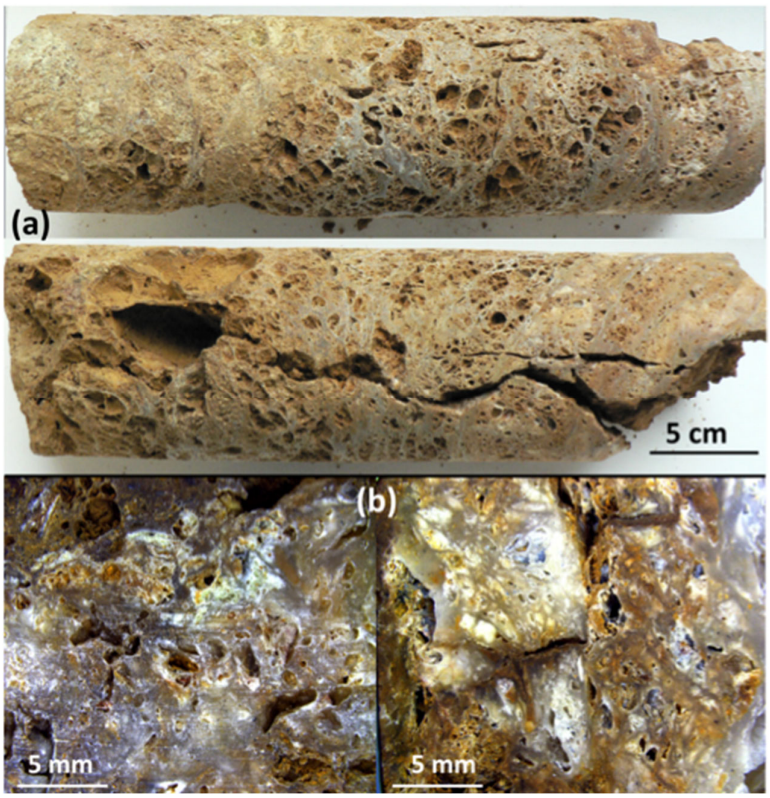

Figure 1. (**a**) Photographs of the breccia drill cores and (**b**) binocular images of breccia squares studied in this work.

2.4. Analytical Methods

Imaging, mapping, and compositional analysis of SiC polymorphs were performed using scanning electron microscope (SUPRA™ 55 SAPPHIRE; Carl Zeiss, Jena, Germany) equipped with energy dispersive spectrometer (EDS). The measurements were done at 15 kV.

X-ray fluorescence spectra were performed using an Inel Equinox 3500 spectrometer (Inel Equinox 3500, Thermo Fisher Scientific Inc., Waltham, MA, USA), equipped with a Cu microfocus source and an Amptek X-123SDD Silicon Drift Detector placed vertically 10 mm over the sample to ensure high sensitivity even with low-atomic number elements. XRF data were collected with an integration time of 600s.

High resolution X-ray diffraction of breccia sample was performed on a D8 Advance Vario 1 Bruker two-circles diffractometer (θ–2θ Bragg-Brentano scan) (D8 Advance Vario 1, Bruker, Karlsruhe, Germany) using a Cu Kα radiation (λ = 1.54059 Å) selected by an incident beam Ge (111) monochromator (Johansson type) and equipped with a LynxEye detector. XRD diagram is collected at room temperature for 2θ varying from 10° to 100° for 1 s per 0.0105° step (12 h/scan).

The Raman spectra were recorded at room temperature using a DXR Raman microscope (DXR, Thermo Fisher Scientific Inc., Waltham, MA, USA) equipped with a 900 lines/mm diffracting grating. The highest quality spectra (highest signal-to-noise) were obtained using green excitation (532 nm, Nd: YAG laser). Raman measurements were carried out at low laser power (1 mW) and with a 100× magnification long working distance. Raman spectra were collected over a range of 80–2000 cm^{-1} (systematically recorded twice with an integration time of 60 s). The spectral region 3300–4000 cm^{-1} was investigated for minerals species with expected OH stretching vibration modes. The laser spot diameter was estimated at 0.8 µm. The peak deconvolution was performed with the Origin software. The mineralogical composition was determined by comparing the collected Raman signals with those reported in the ROD database [44].

3. Results

3.1. Major Composition of the Siliceous Breccia

The chemical analyses by X-Ray Fluorescence (XRF) of the breccia surface indicates ~88 wt.% of silica and 1.9 wt.% Fe_2O_3 (as total iron). Traces of CaO and MgO (0.1 and 0.7 wt.%, respectively) are also present. In term of elemental composition, XRF indicate the presence of Si, Mg, Fe, and other trace elements such as Ni and Cr (Table 1).

Table 1. Elemental composition of breccia in weight, as obtained from XRF measures.

Element	Composition (wt.%)
O	42.7 ± 1.5
Si	25.3 ± 0.8
Mg	21.7 ± 0.8
Fe	4.9 ± 0.4
Ni	0.6 ± 0.2
Al	1.1 ± 0.1
Ca	1.0 ± 0.1
Cr	1.2 ± 0.1
Na	1.25 ± 0.2
K	0.20 ± 0.02

X-ray diffraction pattern (Figure 2) of breccia samples only exhibits the signature of highly crystalline quartz (100 wt.%). The Rietveld refinement performed with a trigonal space group $P3_221$ converged to quartz lattice parameters of a = 4.916 Å and c = 5.408 Å with a mean crystallite size of 161 nm and the microstrain of 8×10^{-4} rms. These refined lattice parameters are very close to that reported in literature [45]. The general R-factors which indicate the overall goodness of fit between the model and experimental data are:

Rwp = 6.3% and Rb = 5.6%, giving goodness of fit of 1.3. It is important to note that no other phase was detected by XRD even though EDS and XRF analysis indicate the presence of 5–7% of iron and other elements. However, the mineral species potentially formed by such elements are not detected by XRD because they are present at very low concentrations (<3%).

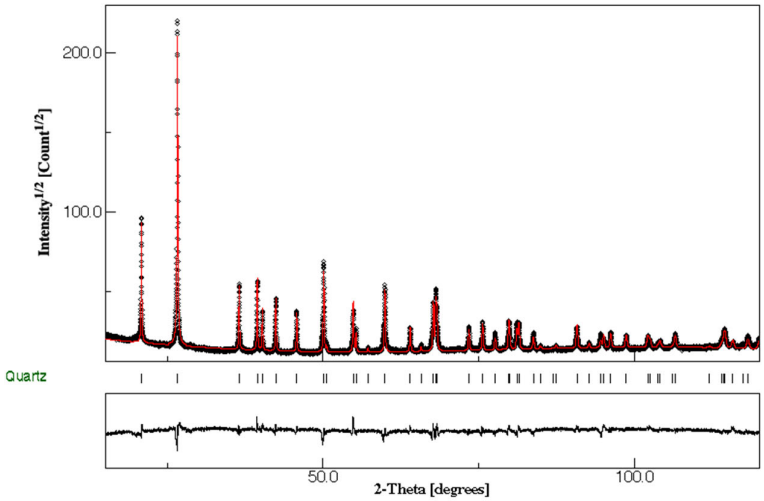

Figure 2. X-ray powder diffraction pattern of breccia sample and corresponding MAUD refinement (MAUD: Material Analysis Using Diffraction, refinement software, http://maud.radiographema.eu/ (accessed on 10 January 2021)). Calculated (red line) and observed patterns (coarse line) are shown. The difference curve ($I_{obs} - I_{calc}$) is shown at the bottom.

Iron is within 5–7 wt.% and is related to iron oxides and oxyhydroxide (hematite, maghemite, magnetite and goethite) present in the quartz matrix as micro to nano-inclusions (Figure 3b). Raman analyses of the breccia matrix confirm that quartz is predominant. The well-defined and mostly narrow Raman bands of quartz attested to its highly crystalline form (Figure 3a). Raman spectroscopy also evidences the presence of serpentine minerals (Figure 3c), lizardite and chrysotile, which crystallized in densely packed fibers. Forsterite, hedenbergite and yellow saponite occur as clots scattered throughout the fine-grained matrix (Figure 3d). Minor phases, e.g., anatase, pyrite and apatite were also observed (Figure 3e). The microfractures in the breccia (Figure 3f–h) are filled with calcite and kerolite 'Ni-rich talc' [33].

The kerolite is the only Ni-bearing phase. The vibrational modes observed for kerolite (Figure 3h) are slightly shifted toward lower wavenumbers compared to pure talc [46] suggesting high Ni substitution in Mg-talc [47]. However, kerolite and Ni-rich talc exhibit three main bands on similar positions (674, 188 and 108 cm^{-1}). In the high wavenumber range (3500–3750 cm^{-1}), the vibrations of the OH groups can be used to discriminate the talc-like phases: the positions and relative intensities of OH contributions are controlled by the types and number of crystallographically equivalent OH groups sites, and by the types of cation occupancies around OH sites, as well as the probabilities of these occupancies.

For Mg-talc, only a strong OH stretching band is expected around 3675 cm^{-1} and for Ni-talc-like (kerolite), the spectrum shows three Ni^{2+} additional vibrations at 3654, 3625, and 3610 cm^{-1} [23,47]. These bands correspond to OH bonded to 2Mg + 1Ni, 1Mg + 2Ni, and 3 Ni, respectively [23,47]. The intensity of the vibration is proportional to the amount of the cation configuration (in our case 3Mg (20.8%), 2Mg + 1Ni (62.4%), 1Mg + 2Ni (1.7%), and 3 Ni (15.1%). This result thus confirmed the presence of high Ni substitution in Mg-talc.

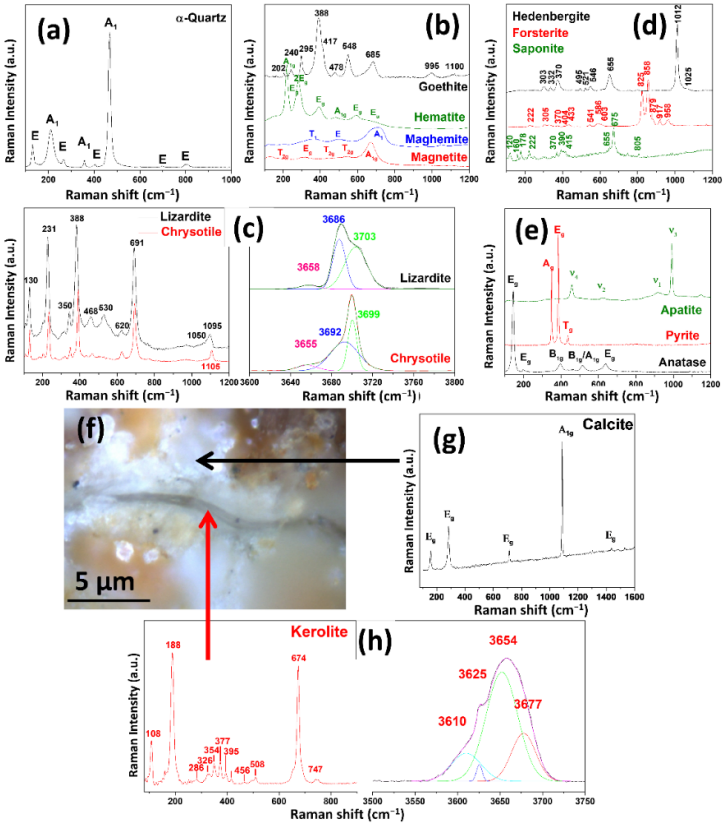

Figure 3. Raman spectra of phases present in the breccia core samples (**a**) α-Quartz (SiO_2), (**b**) Microparticles of iron oxides [hematite (α-Fe_2O_3), maghemite (γ-Fe_2O_3), magnetite (Fe_3O_4)] and goethite (α-FeOOH), (**c**) Lizardite and chrysotile $(OH)_3Mg_3[Si_2O_5(OH)]$, (**d**) Hedenbergite ($CaFeSi_2O_6$), forsterite (Mg_2SiO_4) and saponite $(Ca_{0.25}(Mg,Fe)_3((Si,Al)_4O_{10})(OH)_2{\cdot}n(H_2O))$, (**e**) Pyrite ($FeS_2$), apatite $(Ca_5(PO_4)_3OH)$ and anatase (TiO_2) crystals, (**f**) Optical images of the breccia vein with corresponding Raman spectra of: (**g**) Calcite ($CaCO_3$) and (**h**) Kerolite $((Mg,Ni)_3Si_4O_{10}(OH)_2{\cdot}H_2O)$.

3.2. Pore Fillings in the Siliceous Breccia

Micrometric porosities observed by optical microscopy (Figure 4a,b) incorporate small crystals and clusters of crystals varying from blue to white and colorless-transparent (Figure 4a). Interestingly, micro-Raman measurements on these clusters reveal the presence of chromite and SiC (Figure 4g). SiC (moissanite) occurs either as single grains (approximated size: 5 × 8 × 10 µm^3), sometimes having light blue color to green and colorless irregular flakes or fragments of 10–25 µm (Figure 4c). EDS analyzes on this moissanite crystal indicate C, 48.7 ± 1.9 at. wt.% and Si, 51.3 ± 1.6 at. wt.% (Figure 4d). Although EDS is not accurate for low atomic number elements and not recommended as a technique for the quantification of elements lighter than Na, EDS analyses of moissanite showed that the crystals contained no elements heavier than carbon and Si.

The SiC grain in Figure 4b was selected for a full single crystal diffraction, SCXRD (Figure 5). This SiC grain crystallizes in the space group Cmc21 with 36 atoms per unit cell [a = 3.0778(6) Å, b = 5.335(2) Å, c = 15.1219(6) Å, α = 90°, β = 90°, γ = 120°]. Reflection's splitting can be evidenced in some experimental frames and could be attributed to twinning features. Data were then integrated. The different attempts of integration of reflections using the previous unit cell were not satisfactory: the internal reliability factor R_{int} = 35%, quantifying the symmetry deviation from the intensity of the reflections expected to be equivalent, excludes unambiguously the hexagonal or trigonal symmetries. The reciprocal space was then interpreted in a different way by considering the orthorhombic unit cell and twin components related by a tri-fold axis parallel to c with an internal reliability R_{int} of 7.4%. The structure has been determined by charge in the Cmc21 space group and then

refined. The final agreement factor is Rf = 0.0329(2) for 194 reflections with 20 refinement parameters and $I \geq 3\sigma(I)$.

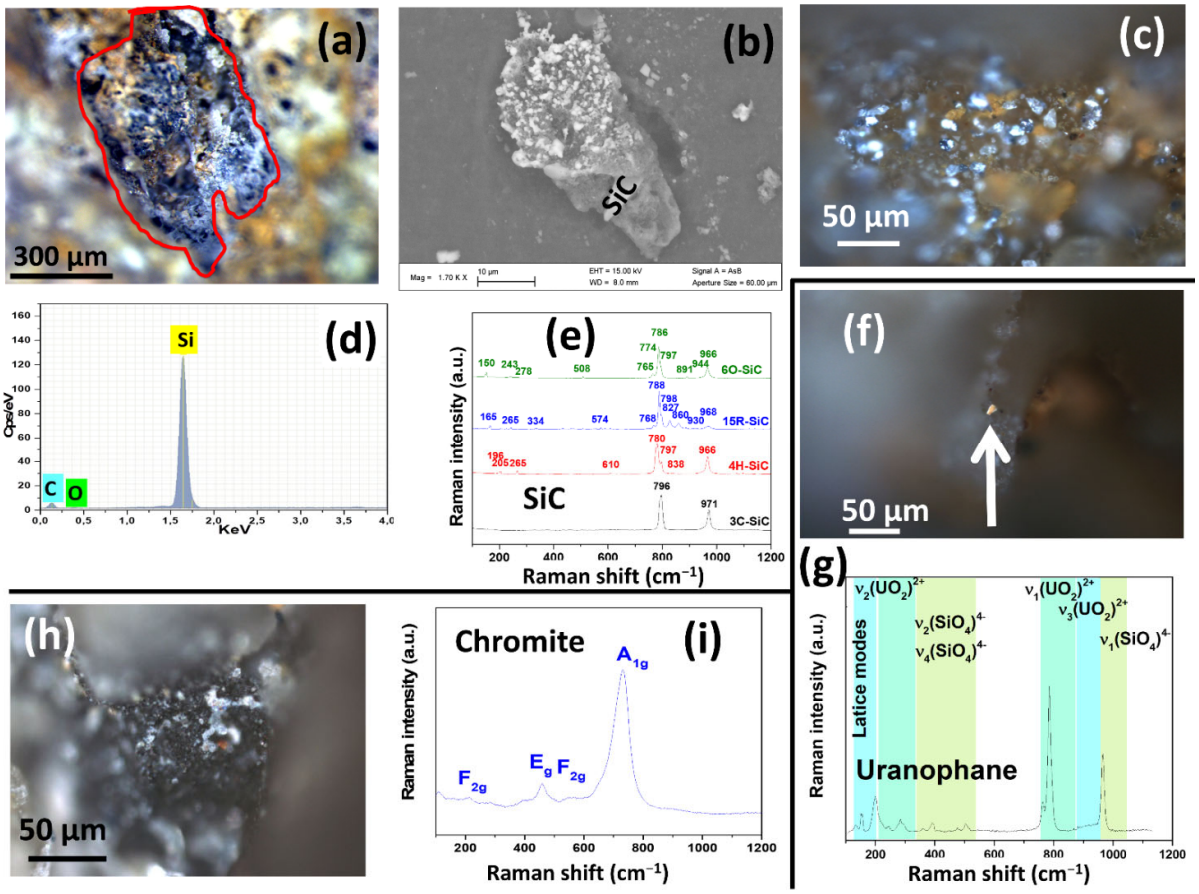

Figure 4. Porosities of siliceous breccia (ER-NC00-0001) (**a**) Optical images of porosities, (**b**) Scanning electron microscope (SEM) image showing a cluster composed of SiC, (**c**) Optical images of various SiC crystals with different colors, (**d**) EDS spectrum of SiC, (**e**) Raman spectra of various SiC crystals with different colors, (**f**) optical images of uranophane, (**g**) Raman spectrum of uranophane, (**h**) optical images of chromite matrix bearing SiC and diamond and (**i**) Raman spectrum of chromite.

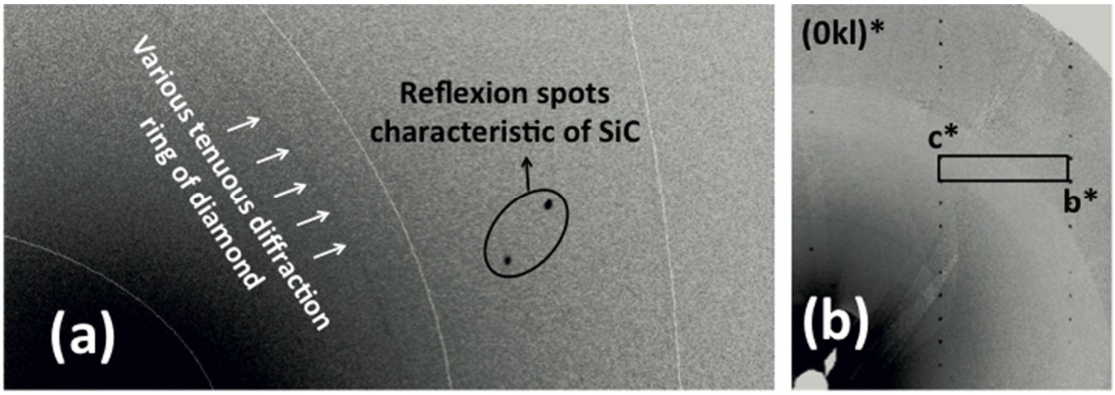

Figure 5. SCXRD of 6O-SiC grain (**a**) Experimental frame exhibiting SiC diffraction spot and (**b**) Part of the (0kl)* reciprocal plan of SiC assembled from the whole experimental frames.

A view of the structure is proposed in Figure 6a. The main characteristics of the 6H-SiC polytype can be observed. The structure can be described from SiC4 tetrahedra all sharing their neighbour edges. El Mendili et al. [17] showed that 6O-SiC results from the 6H-SiC

wurtzite to 3C-SiC rock-salt phase transformation as an intermediate state. The 6O-SiC formation requires at least 4 GPa of pressures and high temperatures 2027–2527 °C.

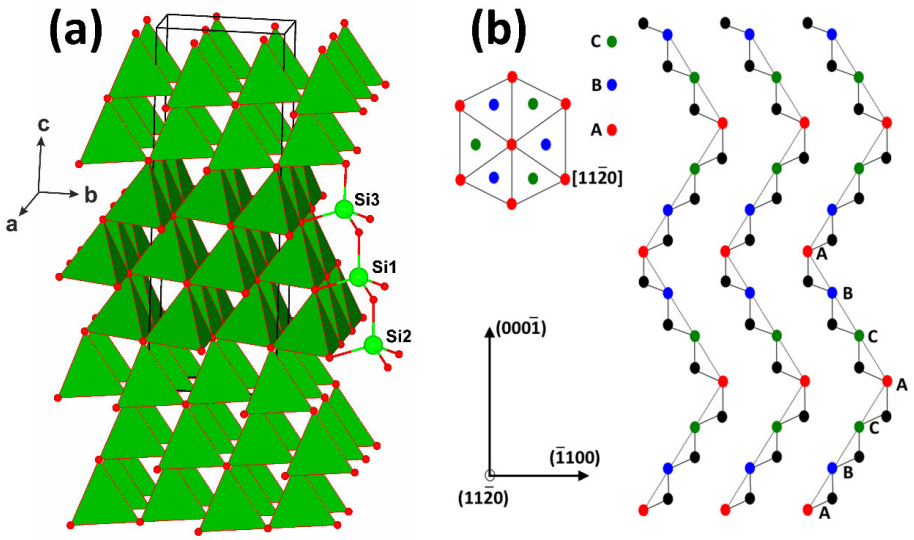

Figure 6. (**a**) Crystal structure refined for the orthorhombic 6O-SiC and (**b**) Stacking sequence of 6O-SiC in the [1120] plane.

Many SiC polytypes exist. They show differences in the stacking sequences of double atomic planes of Si-C along the c-direction. The most common polytypes are 3C, 2H, 4H, 6H, 8H, 9R, 10H, 14H, 15R, 19R, 20H, 21H, and 24R [48]. The three more frequent naturally occurring ones are the cubic 3C (β-type), hexagonal 4H and 6H polytypes. The Raman spectra of SiC polytypes (Figure 4e) show four of the SiC polytypes (3C, 4H, 6O and 15R) [49]. Vibrational bands attributions of SiC polytypes (3C, 4H and 15R) are summarized in the Table 2.

Table 2. Raman shifts of the SiC vibration bands shown in Figure 4e, with reference to [50].

Polytype	Phonon Modes–Frequency (cm^{-1})			
	Transversal Optic TO	Transversal Acoustic TA	Longitudinal Optic LO	Longitudinal Acoustic LA
3C	796	-	971	-
4H	797 780	196 205 256	838 966	610
15R	798 768 788	150 256	860 930 968	334 574

For all the SiC polytypes [50], the Raman modes consist of transverse acoustic and optical phonons (TA, TO), longitudinal acoustic and optical phonons (LA, LO) and longitudinal acoustic phonons (LA). In the case of 3C-SiC, only two strong Raman bands are observed, at 972 cm^{-1} attributed to the longitudinal optical phonon (LO) and at 796 cm^{-1} attributed to the transverse optical phonon mode (TO). In the case of 6H-SiC, the experimental characteristic phonon modes are assigned as follow [50]: E_2(TA) at 151 cm^{-1}, E_1(TA) at 240 cm^{-1}, A_1(LA) at 504 cm^{-1}, E_2(TO) at 762 and 783 cm^{-1}, E_1(TO) at 791 cm^{-1} and A_1(LO) at 887 and 963 cm^{-1}, respectively. For SiC in the siliceous breccia, the main Raman peaks were confirmed and matched with Raman-active vibrational modes of orthorhombic SiC structure with Space Group C*mc*2_1 [17].

Concerning diamond, a series of polytypes are described and predicted in literature [51–54]. Two of them are observed in natural fabrics, the 3C (cubic diamond) and 2H (hexagonal lonsdaleite) diamond.

The Raman spectra of natural breccia diamonds show a sharp, first order peak of sp^3-bonded carbon centered between 1331.4 and 1318 cm^{-1} (Figure 7) with FWHM (Full Width at Half Maximum) from 4.9 to 7.3 cm^{-1}, respectively. Only the 1100–1500 region is illustrated since no other vibrational mode was observed in the region from 60 to 4000 cm^{-1}. Furthermore, no graphite was detected in our samples.

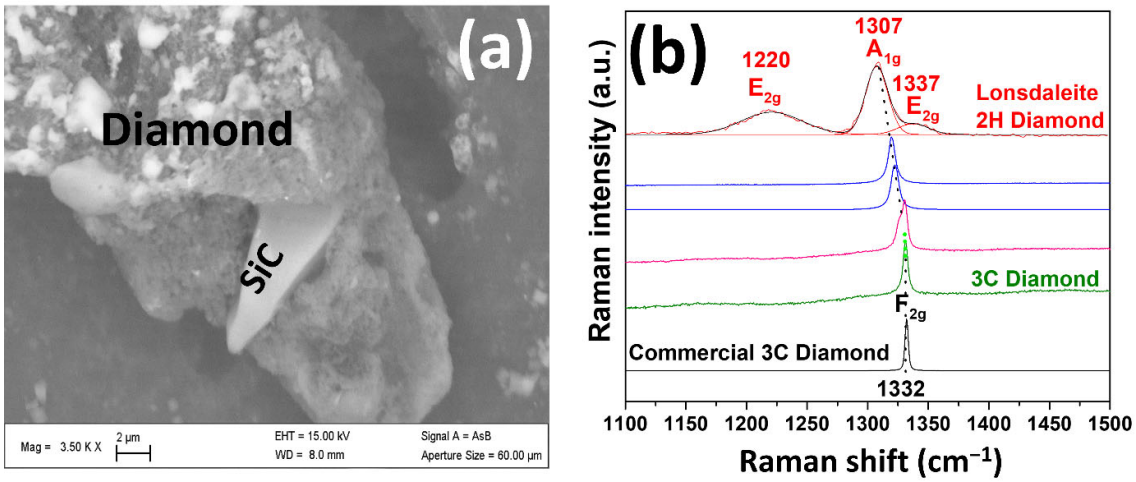

Figure 7. (**a**) Scanning electron microscope (SEM) image showing a cluster composed of SiC and diamond polytypes and (**b**) Raman spectra of five different diamonds from different zones and one commercial cubic diamond.

From literature, it is admitted that the well-crystallized cubic diamond peak is observed at 1332 cm^{-1} and that the sp^3 breathing vibration mode of lonsdaleite (hexagonal diamond) can vary between 1320 and 1327 cm^{-1} [54].

In comparison, a commercial well-crystallized cubic diamond exhibits sp^3 mode centered at 1332 cm^{-1} with a FWHM of 3 cm^{-1}. This value corresponds to one of the spectra observed in Figure 7 (1331.0 $\pm$ 0.5 cm^{-1} with a FWHM of 4.9 $\pm$ 0.1 cm^{-1}). The slightly larger FWHM is related to a slightly lower crystallinity of the natural cubic diamond.

Raman spectrum (Figure 7, pink) exhibiting two overlapped bands was recorded, the first at 1330.5 $\pm$ 0.2 cm^{-1} corresponding to cubic symmetry and the second at 1326.2 $\pm$ 0.2 cm^{-1} assigned to hexagonal diamond. Under the microscope, we could not distinguish individual crystals, and these two contributions can be due to the existence of distorted crystals or to the presence of some sub-micrometric diamond inclusion pockets.

For the sp3 in the 1320–1327 cm^{-1} region, the spectra can be attributed to hexagonal diamond polytypes. Indeed, Authors in [54] earlier interpreted Raman spectra of impact diamond-bearing rocks containing the most intense band within 1320–1327 cm^{-1} as the lonsdaleite contribution. The presence of lonsdaleite in their samples was also confirmed by X-ray diffraction.

In (Figure 7, blue), spectra with the sp3 mode at values below 1320 cm^{-1}, were observed. Authors in [55] suggested that this shift is due to stacking faults of diamond structure, leading to the cubic-hexagonal transition. This structural change from cubic to hexagonal can be explained as the change of stacking sequence of the (111) plane. The FWHM values ranging from 6.4 to 7.3 cm^{-1} are also larger, as expected, than those of cubic diamond. We can then hypothesize that the hexagonal structure is kept in these diamonds, however with some distortions explaining its slightly lower Raman shift and its larger FWHM. Finally, (Figure 7, brown) shows a Raman spectrum with three Raman-active vibrational modes around 1212, 1307 and 1328 cm^{-1}. This spectrum is similar to those reported for lonsdaleite [56].

In literature, although the theoretical calculations of the lonsdaleite vibration spectrum have been the subject of many investigations for years, several ambiguities and contradictions remain present for the vibrational attribution and the position of the bands [56–58].

For this reason, the Raman-active vibrational modes of cubic and hexagonal diamonds were calculated through Density Functional Theory (DFT). We have used the CRYSTAL software [59]. We performed these calculations applying harmonic approximation at the Γ point as it was done by [56]. for Raman identification of lonsdaleite. We have found for cubic diamond that the position of single Raman vibration band, corresponding to the first order scattering of F_{2g} symmetry, is 1331.99 cm^{-1}. This value is in good agreement with the experimental value. For hexagonal diamond (2H, lonsdaleite), we predict three fundamental vibrational modes: 1207 cm^{-1} (E_{2g}), 1307 cm^{-1} (A_{1g}), and 1330 cm^{-1} (E_{1g}). The theoretical intensity ratio of the Raman modes is: 0.5(E_{2g}):1(A_{1g}):0.3(E_{1g}). Hence, the A_{1g} mode is expected to be the most intense line in the Raman spectrum of lonsdaleite.

Based on the comparison between calculated and experimental results (Figure 8), the most intense band in the experimental Raman spectrum at 1307 cm^{-1} can be attributed unambiguously to the longitudinal optical vibrational mode A_{1g}.

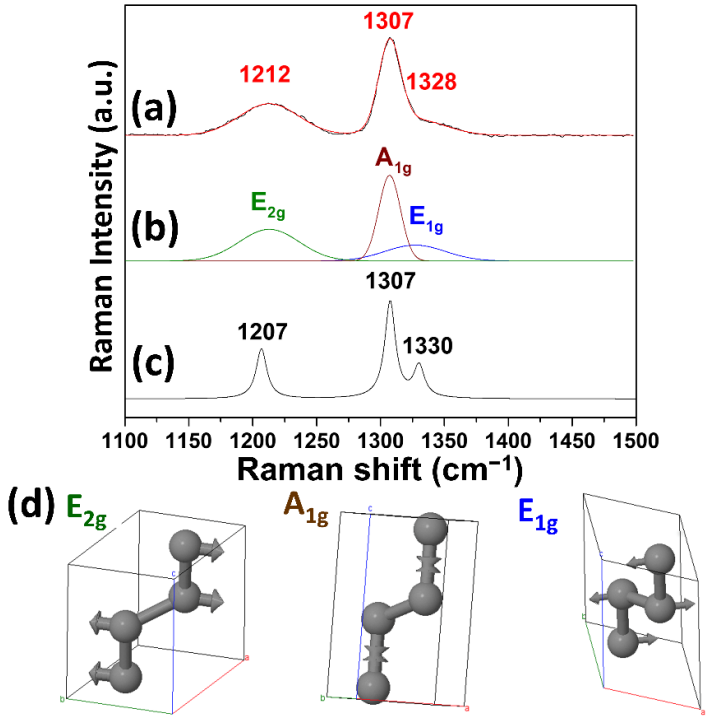

Figure 8. Raman spectrum of lonsdaleite (**a**) Experimental Raman spectrum of lonsdaleite zoomed from (Figure 2f), (**b**) The three Raman-active vibrational modes E_{2g}, A_{1g} and E_{1g} obtained via deconvolution of the experimental spectrum, (**c**) Theoretical Raman spectrum of lonsdaleite obtained through ab initio calculations with Lorentzian line shape and FWHM of 10 cm^{-1} and (**d**) The three Raman vibration modes of lonsdaleite.

The deconvolution analysis of the Raman spectrum let us identify the shoulder as a Raman contribution of the second intensity of the transverse optical vibrational mode (E_{2g}) observed at 1212 cm^{-1}. This agrees with our ab-initio calculations. DFT calculations also predict that the third Raman-active mode of lonsdaleite E_{1g} (transverse optical) should be observed at 1330 cm^{-1}, with its theoretically predicted intensity being close to that of the second intensity mode E_{2g}. The E_{2g} mode is observed in our spectrum around 1328 cm^{-1}.

Experimentally, the lonsdaleite bands are highly broadened (FWHM are in the range of 18–52 cm^{-1}), compared to the cubic diamond observed in our sample. This effect is due to lonsdaleite imperfection and to small dimensions of crystallites.

The originality of these results comes from the fact that lonsdaleite has been observed so far only in the meteorite from the Meteor Crater [51,56]. Probable contribution of other hexagonal diamond polytypes to Raman spectra can be masked by the presence of large and asymmetric bands [54].

In Figure 4g, the Raman spectrum of chromite shows four bands associated to the CrO bond-stretching region at 905, 730, 560 and 445 cm^{-1} [60]. The very intense and broad band at 730 cm^{-1} is assigned to symmetric stretching vibrational mode, $A_{1g}(\nu_1)$. The two peaks at 560 and 445 cm^{-1} are attributed to $F_{2g}(\nu_4)$ and $E_g(\nu_2)$ modes respectively, and the small band at 215 cm^{-1} to the $F_{2g}(\nu_3)$ mode.

Uranophane was unambiguously determined in the Raman spectrum shown in Figure 4f containing the characteristic bands reported in [61,62]. The identification of the different secondary phases is based on the analysis of the symmetrical stretching vibration of the uranyl group UO_2^{2+}, which allows the identification of individual uranyl phases and can be used as a fingerprint. For uranyl, two Raman bands close to 790 and 800 cm^{-1} are attributed to the doubly degenerate ν_1 mode of UO_2^{2+} symmetric stretching modes, while a weak band close to 919 cm^{-1} is assigned to the $\nu_3(UO_2^{2+})$ anti-symmetric stretching vibrations, and the bands in the 200–300 cm^{-1} are assigned to $\nu_2(UO_2^{2+})$ symmetric bending mode and to UO ligand vibration [63]. Multiple bands in this region indicate the non-equivalence of the UO bonds and the lifting of the degeneracy of $\nu_2(UO_2^{2+})$ vibrations. In addition, the band at 148 cm^{-1} is attributed to lattice mode. Raman spectrum shows the expected $\nu_2(SiO_4^{4-})$ and $\nu_4(SiO_4^{4-})$ symmetric bending modes at 485 and 510 cm^{-1}, respectively. The anti-symmetric stretching modes $\nu_1(SiO_4^{4-})$ is present at 970 cm^{-1}. Figure 9 shows the SEM image and the chemical composition (EDS) of the uranium rich zone. The observation of uranium, silicon and calcium in the EDS spectrum is clear evidence of the presence of U-Ca-silicate.

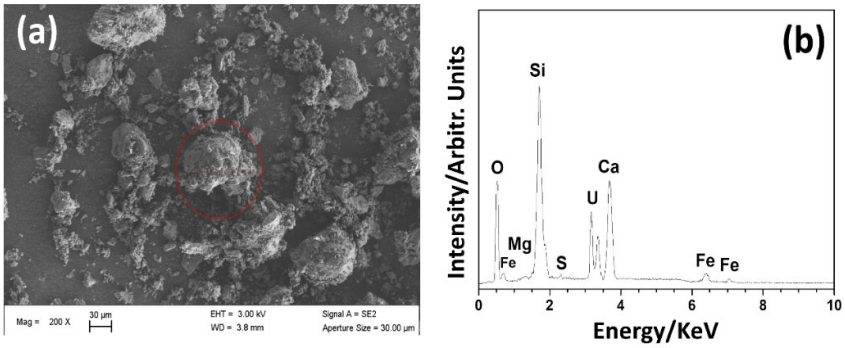

Figure 9. Ca-Uranyl silicate. (**a**) SEM image and (**b**) EDX spectrum.

4. Discussion

Siliceous breccia, or vuggy silica is described from laterite profiles world-wide, such as in the Nickel Mountain, Sierra Nevada, Douglas County, Oregon, or the Klamath Mountains [64,65]. At the Tiébaghi Mine (New Caledonia), the siliceous breccia is widespread along the saprolite, and was formed after saprolitization as it hosts saprolite fragments [20]. High hydraulic conductivity in the saprolite (8.10^{-7}m/s) [41] and meteoric water circulation is the origin of this siliceous breccia. The presence of trace amounts of olivine and the Ca-bearing pyroxene (hedenbergite) suggests additional serpentinization reactions. Saponite is an important compound in this saprolite. It was detected in the silica matrix in this study. Dissolution of saponite generates high amounts of silica: 18 saponite (Mg) + 23 H_2O = 19 serpentine + 6 diaspore + 28 SiO_2 (aq). This hydration reaction is exothermic [66,67], and may have just let to temperature increase as suggested by [43]. Saprolite is composed of a mixture of serpentines, clay minerals, and oxides. Saponite dissolution is pH dependent. Laboratory experiments have shown that at acidic pH = 3, silica is massively produced. For the Tiébaghi siliceous breccia formation, we suggest that most likely reaction (2) and (3) may be responsible for the silica generation. The dissolution of

saprolite leads to the formation of cavities. These cavities are then filled by the porous breccia at Tiébaghi. For the sudden precipitation of massive porous micro-quartz in the saprolite horizon, one possible model is the precipitation due to a sudden change of pH of the aqueous fluids. The water resurgences at the base of the aquifers are basic with a pH up to 11 [68], whereas pH in coarse saprolite level is around ~8 [33].

Before discussing the origin of diamond and the associated strongly reducing phases appearing in the pores of the breccia, we argue against that these phases are artefacts, generated during sample preparation through diamond sawing: (i) the sample preparation was carried out identically for the three other rocks (sandstone, harzburgite, granite), all sawn with the same diamond blade [22]. (ii) all the samples were studied by micro-Raman spectroscopy [22,23], but only the siliceous breccia hosts diamond polymorphs. (iii) the intergrowth of diamond and lonsdaleite is unlikely being a feature for diamond saw derived particles. (iv) clusters of chromite, diamond and SiC polymorph are observed in natural environment [2,5,28,31]. Therefore, the idea of contamination was ruled out.

Diamonds and exotic minerals such as moissanite (SiC) and metal alloys were described from different ophiolite environments (e.g., Luobusa ophiolite (Tibet), in the early Paleozoic Ray-Iz ophiolite (polar Ural, Russia); Pozanti-Karsanti ophiolite, Eastern Tauride belt, southern Turkey, Mao Baracoa Ophiolite, Cuba and the Tehuitzingo ophiolite, Mexico) [2,4,15,16,28,31]. In all these cases, UHP and diamond are associated with peridotites and chromitite. The Tiébaghi nickel laterites were formed on ophiolitic upper mantle serpentinzed peridotites. Serpentinites formed under reducing conditions frequently host metal alloys such as $FeNi_3$ (awaruite), the Fe-rich variety, taenite, or even native Fe [26,69]. Moreover, magnetite and chromite are stable phases under high pH and reducing conditions (fO_2 < FMQ (Fayalite–Magnetite–Quartz–buffer)) [12,65]. Saprolitization, as incipient weathering of serpentinite, still occurs under reducing conditions and alkaline pH (around 8) as serpentine (formed during weathering) and smectite are stable. Both phases are major Fe and Ni carriers. An organic matter and nickel-sulfide rich horizon (so called gley) even occurs at the interface between yellow laterite and saprolite [65].

At Tiébaghi, the largest chromium mine in the world operated in 1941 produced about 54,000 tons per year with an overall production of 3.3 million tons of Cr-rich lumpy chromite within 88 years (1902–1990). Cr-spinel is detected in the siliceous breccia and can be interpreted as relicts having survived serpentinization and saprolitization of the peridotites under alkaline conditions. Based on point analyses, the Cr-spinel detected in the siliceous breccia show high Cr# typical for chromite from boninitic melts. Thi finding is in agreement with studies by [68] showing that lherzolite from at Tiébaghi and Poum presents a refertilized harzburgite having experienced an interaction with a boninitic melt [68].

Associated with the Cr-rich spinels in the siliceous breccia, diamond including lonsdaleite and moissanite as 6O-SiC occur. Different models were proposed to explain the diamond and moissanite occurrence in ophiolites, based on C-isotopic compositions, trace element studies on diamonds and diamond inclusion mineralogy [4,15,16]. Moissanite xenocrysts in chromitite are suggested being originated from a deep mantle source in the Luobusa ophiolite, as chromite crystals represent coesite lamellae [70]. Organic carbon derived from the subduction slab was proposed as C source as the involvement of high temperature fluids, such as second stage melts [71]. New results, based on mineralogical studies on microdiamonds from ophiolites in Cuba and Mexico [4,15,16], and thermodynamic calculation by McCollom and Bach [72] supports a low- pressure origin of microdiamonds.

In nature, lonsdaleite is mainly associated with cubic diamond. It can form under ultra-high pressures (>130 kbar), at depths > 150 km, at temperatures above 950 °C at PO_2 close to IW (Iron-wüstite) [73,74]. Since it is described from meteorites and rocks having experienced shock metamorphism [75], intensive studies have been performed [76]. Lonsdaleite is difficult to analyze as is always tightly intergrown with diamond, sometimes graphite, and is of submicrometric size [76]. These phases often present dislocations, stacking faults, twins, and grain boundary disordering. Therefore, microanalysis and

structural interpretations of XRD and TEM-SAED (transmission electron microscopy (TEM), selected area electron diffraction (SAED)) may be erroneous due to fuzzy spectra [77].

In this study, analyzes of spectral data from micro-Raman spectroscopy were compared and supplemented by results from DFT. This methodology allowed unambiguously to identify lonsdaleite and cubic diamond. The mineral association (lonsdaleite, moissanite, chromite, native chromium) observed in the unaltered chromitite and peridotite from the above-mentioned localities is like that observed in the siliceous breccia from the Tiébaghi mine [4]. The moissanite described from peridotites and chromitites in ophiolites are mainly subhedral to anhedral, similarly to those observed in the siliceous breccia pores at Tiébaghi [4].

At Tiébaghi, not only microdiamonds were detected but also lonsdaleite and moissanite Our data set is not sufficient to conclude on the ultimate origin of these reducing phases. However, we suggest that these phases are inherited from the serpentinized peridotites. Further studies must be carried out to support a deep or shallow mantle origin. This is beyond the scope of this study.

The uranyl-silicates are the most abundant group of uranyl minerals because of the ubiquity of dissolved Si in most groundwaters. Uranophane is the most common uranyl mineral, precipitating from near neutral to alkaline groundwaters that contain dissolved Si and Ca. Uranophane is a common neoformed mineral derived from the alteration of uraninite (UO_2) [78] in large surroundings of uranium deposits such as in the *Koongarra* deposit (Australia) [79]. At this location uranium mineralization occurs in breccia and associated faults surrounding the breccia. This is related to the high mobility of uranium in oxidizing environments due to U(VI) formation.

Uranyl silicates are formed in the surface of uraninite under oxidizing conditions [80–83]. However, the direct precipitation of uranophane, as observed in the siliceous breccia in this study, requires a high concentration of Si in solution [80,82]. The stabilization of uranophane in high silica, high pH and Ca^{2+} bearing environments is also documented [80,82].

The origin of the uranium in the siliceous breccia, can be only roughly discussed, as no uranium mineralization is known in New Caledonia. Uranium bearing minerals, such as apatite was detected by micro-Raman analyses in this study. Apatite commonly contains several tens to hundreds of ppm of uranium [83]. However, under the above-mentioned conditions, apatite tends to be stable [84], which makes such an origin unlikely. At Tiébaghi, pegmatitic dykes crosscutting the laterite profile are described [28]. However, no petrographical study on these rocks is published so far. These rocks need to be further investigated as pegmatites may host uranium and uranium bearing accessory minerals.

5. Conclusions

In this paper, we reveal for the first time the association of SiC and diamondpolytypes, chromite and uranophane in a nickel laterite profile at Tiébaghi (New Caledonia), unambiguously defined by Micro Raman spectroscopy and XRD. The diamond and moissanite polytypes are inherited from serpentinized peridotites.

Based on these studies, the breccia at Tiébaghi needs to be further investigated and may present exploration potential, as it acts as a trap for weathering-resistant valuable minerals, and elements migrating in low temperature silica rich environments, such as U, Ni, Cr.

This study also highlights the potential and importance of micro-Raman spectroscopy to achieve the structural properties of porous materials. This technique is thus crucially important for mining companies to rapidly access detailed mineralogical compositions without any sample preparation.

Author Contributions: Conceptualization, Y.E.M., B.O., D.C. and S.G.; methodology, Y.E.M., B.O., D.C., J.-F.B., S.G., S.P. and O.P.; software, Y.E.M., D.C., J.-F.B., S.G., S.P. and O.P.; validation, Y.E.M., B.O. and D.C.; formal analysis, Y.E.M., B.O., D.C., J.-F.B. and S.G.; investigation, Y.E.M., B.O., D.C., J.-F.B., S.G., S.P. and O.P.; resources, Y.E.M., B.O. and D.C.; writing—original draft preparation, Y.E.M.,

D.C., J.-F.B. and S.G.; writing—review and editing, Y.E.M., D.C., J.-F.B. and S.G.; visualization, Y.E.M., D.C., J.-F.B. and S.G.; All authors have read and agreed to the published version of the manuscript.

Funding: This research was funded by the European Commission in the frame of the SOLSA project (H2020 program): SC5-11d-689868.

Data Availability Statement: The experimental and computational data presented in the present paper are available from the corresponding author upon request.

Acknowledgments: We thank the SLN for providing the sample material, and the BRGM staff for preparing the samples.

Conflicts of Interest: The authors declare no conflict of interest.

References

1. Gevorkyan, R.G.; Kaminsky, F.V.; Lunev, V.C.; Osovetsky, V.M.; Nachatryan, N.D. A new occurrence of diamonds in ultramafic rocks in Armenia. *Dokl. AN Armen. SSR* **1976**, *63*, 176–181.
2. Lian, D.; Yang, J.; Dilek, Y.; Wu, W.; Zhang, Z.; Xiong, F.; Liu, F.; Zhou, W. Deep mantle origin and ultra-reducing conditions in podiform chromitite: Diamond, moissanite, and other unusual minerals in podiform chromitites from the Pozanti-Karsanti ophiolite, southern Turkey. *Am. Mineral.* **2017**, *102*, 1101–1113.
3. Moe, K.S.; Yang, J.S.; Johnson, P.; Xu, X.; Wang, W. Spectroscopic analysis of microdiamonds in ophiolitic chromitite and peridotite. *Lithosphere* **2018**, *10*, 133–140. [CrossRef]
4. Pujol-Solà, N.; Proenza, J.A.; Garcia-Casco, A.; González-Jiménez, J.M.; Andreazini, A.; Melgarejo, J.C.; Gervilla, F. An Alternative Scenario on the Origin of Ultra-High Pressure (UHP) and Super-Reduced (SuR) Minerals in Ophiolitic Chromitites: A Case Study from the Mercedita Deposit (Eastern Cuba). *Minerals* **2018**, *8*, 433. [CrossRef]
5. Trumbull, R.B.; Yang, J.S.; Robinson, P.T.; Di Pierro, S.; Vennemann, T.; Wiedenbeck, M. The carbon isotope composition of natural SiC (moissanite) from the Earth's mantle: New discoveries from ophiolites. *Lithos* **2009**, *113*, 612–620. [CrossRef]
6. Gorshkov, A.I.; Titkov, S.V.; Bao, Y.N.; Ryabchikov, I.D.; Magazina, L.O. Microinclusions in diamonds of octahedral habit from kimberlites of Shandong Province, Eastern China. *Geol. Ore Deposit.* **2006**, *48*, 326–334. [CrossRef]
7. Di Pierro, S.; Gnos, E.; Grobety, B.H.; Armbruster, T.; Bernasconi, S.M.; Ulmer, P.J.S. Rock-forming moissanite (natural alpha-silicon carbide). *Am. Mineral.* **2003**, *88*, 1817–1821. [CrossRef]
8. Bai, W.; Robinson, P.T.; Fang, Q.; Yang, J.; Yan, B.; Zhang, Z.; Hu, X.-F.; Zhou, M.-F.; Malpas, J. The PGE and base-metal alloys in the podiform chromitites of the Luobusa ophiolite, southern Tibet. *Can. Mineral.* **2000**, *38*, 585–598. [CrossRef]
9. Xu, S.; Wu, W.; Xiao, W.; Yang, J.; Chen, J.; Ji, S.; Liu, Y. Moissanite in serpentinites from the Dabie Shan Mountains in China. *Mineral. Mag.* **2008**, *72*, 899–908. [CrossRef]
10. Qi, D.; DeYoung, B.J.; Innes, R.W. Structure-Function Analysis of the Coiled-Coil and Leucine-Rich Repeat Domains of the RPS5 Disease Resistance Protein. *Plant Physiol.* **2012**, *158*, 1819–1832. [CrossRef]
11. Bauer, J.; Fiala, J.; Hrichova, R. Natural a-silicon carbide. *Am. Mineral.* **1963**, *48*, 620–634.
12. Schmidt, M.W.; Gao, C.; Golubkova, A.; Rohrbach, A.; Connolly, J.A. Natural moissanite (SiC)—A low temperature mineral formed from highly fractionated ultra-reducing COH-fluids. *Prog. Earth Planet. Sci.* **2014**, *1*, 27–30. [CrossRef]
13. Pearson, D.G.; Davies, G.R.; Nixon, P.H. Geochemical Constraints on the Petrogenesis of Diamond Facies Pyroxenites from the Beni Bousera Peridotite Massif, North Morocco. *J. Petrol.* **1993**, *34*, 125–172. [CrossRef]
14. Davies, G.R.; Nixon, P.H.; Pearson, D.G.; Obata, M. Tectonic implications of graphitized diamonds from the Ronda peridotite massif, southern Spain. *Geology* **1993**, *21*, 471–474. [CrossRef]
15. Pujol-Solà, N.; Garcia-Casco, A.; Proenza, J.A.; González-Jiménez, J.M.; del Campo, A.; Colás, V.; Canals, À.; Sánchez-Navas, A.; Roqué-Rosell, J. Diamond forms during low pressure serpentinisation of oceanic lithosphere. *Geochem. Persp. Let.* **2020**, *15*, 19–24. [CrossRef]
16. Farré-de-Pablo, J.; Proenza, J.A.; González-Jiménez, J.M.; Garcia-Casco, A.; Colás, V.; Roqué-Rossell, J.; Camprubí, A.; Sánchez-Navas, A. A shallow origin for diamonds in ophiolitic chromitites. *Geology* **2019**, *47*, 75–78. [CrossRef]
17. El Mendili, Y.; Orberger, B.; Chateigner, D.; Bardeau, J.-F.; Gascoin, S.; Petit, S.; Perez, O.; Khadraoui, F. Insight into the structural, elastic and electronic properties of a new orthorhombic 6O-SiC polytype. *Sci. Rep.* **2019**, *10*, 7562. [CrossRef] [PubMed]
18. Lovering, T.G. *Radioactive Deposits in New Mexico*; Geological Survey Bulletin: Reston, VA, USA, 1956; pp. 315–390.
19. Min, M.; Fang, C.; Fayek, M. Petrography and genetic history of coffinite and uraninite from the Liueryiqi granite-hosted uranium deposit, SE China. *Ore Geol. Rev.* **2005**, *26*, 187–197. [CrossRef]
20. Shukla, M.K.; Sharma, A. A brief review on breccia: It's contrasting origin and diagnostic signatures. *Solid. Earth Sci.* **2018**, *3*, 50–59. [CrossRef]
21. Leonardos, O.H.; Fernandes, S.M.; Fyfe, W.S.; Powell, M. The mciro-chemistry of uraniferous laterites from Brazil: A natural example of inorganic chromatography. *Chem. Geol.* **1987**, *60*, 111–119. [CrossRef]
22. Duée, C.; Orberger, B.; Maubec, N.; Laperche, V.; Capar, L.; Bourguignon, A.; Bourrat, X.; Mendili, Y.E.I.; Chateigner, D.; Gascoin, S.; et al. Impact of heterogeneities and surface roughness on pXRF, pIR, XRD and Raman analyses: Challenges for on-line, real-time combined mineralogical and chemical analyses on drill cores and implication for "high speed" Ni-laterite exploration. *J. Geochem. Explor.* **2019**, *198*, 1–17. [CrossRef]

23. El Mendili, Y.; Chateigner, D.; Orberger, B.; Gascoin, S.; Bardeau, J.-F.; Petit, S.; Duee, C.; Guen, M.L.; Pilliere, H. Combined XRF, XRD, SEM-EDS, and Raman Analyses on Serpentinized Harzburgite (Nickel Laterite Mine, New Caledonia): Implications for Exploration and Geometallurgy. *ACS Earth Space Chem.* **2019**, *3*, 2237–2249. [CrossRef]
24. Cassard, D.; Nicolas, A.; Rabinovitch, M.; Moutte, J.; Leblanc, M.; Prinzhofer, A. Structural classification of chromite pods in New Caledonia. *Econ. Geol.* **1981**, *76*, 805–881. [CrossRef]
25. Marchesi, C.; Garrido, C.J.; Godard, M.; Belley, F.; Ferré, E. Migration and accumulation of ultra-depleted subduction-related melts in the Massif du Sud ophiolite (New Caledonia). *Chem. Geol.* **2009**, *266*, 171–186. [CrossRef]
26. Prinzhofer, A.; Allègre, C. Residual peridotite and the mechanism of partial melting. *Earth Planet. Sci. Let.* **1985**, *74*, 251–265. [CrossRef]
27. Moutte, J. Le massif de Tiebaghi, Nouvelle-Calédonie, et ses gites de chromite. Ph.D. Thesis, Ecole Nationale Supérieure des Mines de Paris, Paris, France, 1979.
28. Bailly, L.; Ambrosi, J.P.; Barbarand, J.; Beauvais, A.; Cluzel, D. Nickel-Typologie des latérites de Nouvelle-Calédonie. Gisements de nickel latéritique, volume II. In *Rapport de Recherche: Tome Nickel et Technologie*; HAL: Paris, France, 2014; pp. 1–448.
29. Sevin, B.; Ricordel-Prognon, C.; Quesnel, F.; Cluzel, D.; Lesimple, S.; Maurizot, P. First palaeomagnetic dating of ferricrete in New Caledonia: New insight on the morphogenesis and palaeoweathering of 'Grande Terre'. *Terra Nova* **2012**, *24*, 77–85. [CrossRef]
30. Mc Rae, E. *Nickel Statistics and Information*; Annual Publication; USGS: Reston, VA, USA, 2018.
31. Trescases, J.J. The lateritic nickel-ore deposits. In *Soils and Sediments Mineralogy and Geochemistry*; Paquet, H., Clauer, N., Eds.; Springer: Berlin, Germany, 1997; pp. 125–138.
32. Cathelineau, M.; Myagkiy, A.; Quesnel, B.; Boiron, M.-C.; Gautier, P.; Boulvais, P.; Ulrich, M.; Truche, L.; Golfier, F.; Drouillet, M. Multistage crack seal vein and hydrothermal Ni enrichment inserpentinized ultramafic rocks (Koniambo massif, New Caledonia). *Miner. Depos.* **2017**, *52*, 945–960. [CrossRef]
33. Dublet, G.; Juillot, F.; Morin, G.; Fritsch, E.; Fandeur, D.; Ona-Nguema, G.; Brown, G.E. Ni speciation in a New Caledonian lateritic regolith: A quantitative. X-ray absorption spectroscopy investigation. *Geochim. Cosmochim. Acta* **2012**, *95*, 119–133. [CrossRef]
34. Manceau, A.; Calas, G.; Decarrau, A. Nickel-bearing clay minerals: I. Optical study of nickel crystal chemistry. *Clay Miner.* **1985**, *20*, 367–487. [CrossRef]
35. Cluzel, D.; Meffre, S.; Maurizot, P.; Crawford, A.J. Earliest Eocene (53 Ma) convergence in the Southwest Pacific: Evidence from pre-obduction dikes in the ophiolite of New Caledonia. *Terra Nova* **2006**, *18*, 395–402. [CrossRef]
36. Jeanpert, J.; Lesimple, S.; Sevin, B.; Maurizot, P.; Robineau, B.; Maréchal, J.-C.; Dewandel, B. Exploration des Galeries Chromical-Massif de Tiébaghi. In *Observations Géologiques et Hydrogéologiques à L'intérieur D'un Massif de Péridotites*; SGNC/DIMENC: New Caledonia, France, 2015; pp. 1–35.
37. Lagabrielle, Y.; Chauvet, A.; Ulrich, M.; Guillot, S. Passive obduction and gravity-driven emplacement of large ophiolitic sheets: The New Caledonia ophiolite (SW Pacific) as a case study? *Bull. Soc. Géol. Fr.* **2013**, *6*, 545–556. [CrossRef]
38. Maurizot, P. Formations miocènes de Népoui. In *Compilation des Connaissances*; BRGM-SGNC: Nouméa, France, 2011; pp. 1–96.
39. Maurizot, P.; Cluzel, D. Pre-obduction records of Eocene foreland basins in central New Caledonia: An appraisal from surface geology and Cadart-1 borehole data. *New Zealand J. Geol. Geophys.* **2014**, *57*, 300–311. [CrossRef]
40. Camus, H.; Leveneur, D.; Bart, F. Structuration karstique des aquifères dans les massifs ophiolitiques de Nouvelle-Calédonie. In *Aquifères de Socle: Le Point Sur Les Concepts et Les Applications Opérationnelles*; La Roche-sur-Yon, Pays de la Loire, France, 2015.
41. Jeanpert, J. Structure et fonctionnement hydrogéologiques des massifs de péridotites d Nouvelle-Calédonie. Ph.D. Thesis, Université de la Réunion, Saint-Denis, France, 2017.
42. Trittschack, R.; Grobéty, B.; Koch-Müller, M. In situ high-temperature Raman and FTIR spectroscopy of the phase transformation of lizardite. *Am. Mineral.* **2012**, *97*, 1965–1976. [CrossRef]
43. Guillou-Frottier, L.; Beauvais, A.; Bailly, L.; Wyns, R.; Augé, T.; Audion, A.S. Transient hydrothermal corrugations within mineralized ultramafic laterites. In Proceedings of the SGA Biannual conference, Nancy, France, 24–27 August 2015.
44. El Mendili, Y.; Vaitkus, A.; Merkys, A.; Gražulis, S.; Chateigner, D.; Mathevet, F.; Gascoin, S.; Petit, S.; Bardeau, J.-F.; Zanatta, M.; et al. Raman Open Database: First interconnected Raman-XRD open-access resource for material identification. *J. Appl. Cryst.* **2019**, *52*, 618–625. [CrossRef]
45. Le Page, Y.; Donnay, G. Refinement of the Crystal Structure of Low-Quartz. *Acta Crystallogr. Sect. B Struct. Crystallogr. Cryst. Chem.* **1976**, *32*, 2456–2459. [CrossRef]
46. Neeway, J.; Abdelouas, A.; Ribet, S.; David, K.; El Mendili, Y.; Grambow, B.; Schumacher, S. Effect of Callovo-Oxfordian clay rock on the dissolution rate of the SON68 simulated nuclear waste glass. *J. Nucl. Mater.* **2015**, *459*, 291–300. [CrossRef]
47. Čermáková, Z.; Hradil, D.; Bezdička, P.; Hradilová, J. New data on "kerolite–pimelite" series and the colouring agent of Szklary chrysoprase, Poland. *Phys. Chem. Miner.* **2017**, *44*, 193–202. [CrossRef]
48. Cheung, R. *Silicon Carbide Microelectromechanical Systems for Harsh Environments*; Imperial College Press: London, UK, 2006.
49. Lu, Y.P.; He, D.W.; Zhu, J.; Yang, X.D. First-principles study of pressure-induced phase transition in silicon carbide. *Phys. B.* **2008**, *403*, 3543–3546. [CrossRef]
50. Nakashima, S.; Harima, H. Raman Investigation of SiC Polytypes. *Phys. Status Solidi* **1997**, *162*, 39–64. [CrossRef]
51. Frondel, C.; Marvin, U.B. Lonsdaleite, a hexagonal polymorph of diamond. *Nature* **1967**, *214*, 587–589. [CrossRef]
52. Spear, K.E.; Phelps, A.W.; White, W.B. Diamond polytypes and their vibrational spectra. *J. Mater. Res.* **1990**, *5*, 2277–2285. [CrossRef]
53. Kraus, D.; Ravasio, A.; Gauthier, M.; Gericke, D.O.; Vorberger, J.; Frydrych, S.; Helfrich, J.; Fletcher, L.B.; Schaumann, G.; Nagler, B.; et al. Nanosecond formation of diamond and lonsdaleite by shock compression of graphite. *Nat. Commun.* **2016**, *7*, 10970. [CrossRef]

54. Smith, D.C.; Godard, G. UV and VIS Raman spectra of natural lonsdaleites: Towards a recognised standard. *Spectrochim. Acta Part A Mol. Biomol. Spectrosc.* **2009**, *73*, 428–435. [CrossRef]
55. Nishitani-Gamo, M.; Sakaguchi, I.; Loh, K.P.; Kanda, H.; Ando, T. Confocal Raman spectroscopic observation on hexagonal diamond formation from dissolved carbon in nickel under chemical vapor deposition conditions. *Appl. Phys. Lett.* **1998**, *73*, 765–767. [CrossRef]
56. Goryainov, S.V.; Likhacheva, A.Y.; Rashchenko, S.V.; Shubin, A.S.; Afanas'ev, V.P.; Pokhilenko, N.P. Raman identification of lonsdaleite in Popigai impactites. *J. Raman Spectrosc.* **2014**, *45*, 305–313. [CrossRef]
57. Wu, B.R. Structural and vibrational properties of the 6H diamond: First-principles study. *Diam. Relat. Mater.* **2007**, *16*, 21–28. [CrossRef]
58. Denisov, V.N.; Mavrin, B.N.; Serebryanaya, N.R.; Dubitsky, G.A.; Aksenenkov, V.V.; Kirichenko, A.N.; Kuzmin, N.V.; Kulnitskiy, B.A.; Perezhogin, I.A.; Blank, V.D. First-principles, UV Raman, X-ray diffraction and TEM study of the structure and lattice dynamics of the diamond–lonsdaleite system. *Diam. Relat. Mater.* **2011**, *20*, 951–953. [CrossRef]
59. Dovesi, R.; Orlando, R.; Erba, A.; Zicovich-Wilson, C.M.; Civalleri, B.; Casassa, S.; Maschio, L.; Ferrabone, M.; De La Pierre, M.; D'Arco, P.; et al. CRYSTAL14: A program for the ab initio investigation of crystalline solids. *Int. J. Quantum Chem.* **2014**, *114*, 1287–1317. [CrossRef]
60. Reddy, B.J.; Frost, R.L. Spectroscopic characterization of chromite from the Moa-Baracoa Ophiolitic Massif, Cuba. *Spectrochim. Acta Part A: Mol. Biomol. Spectrosc.* **2005**, *61*, 1721–1728. [CrossRef]
61. Driscoll, R.J.P.; Wolverson, D.; Mitchels, J.M.; Skelton, J.M.; Parker, S.C.; Molinari, M.; Khan, I.; Geeson, D.; Allen, G.C. Raman spectroscopic study of uranyl minerals from Cornwall, UK. *RSC. Adv.* **2014**, *4*, 59137–59149. [CrossRef]
62. Bonales, L.J.; Menor-Salván, C.; Cobos, J. Study of the alteration products of a natural uraninite by Raman spectroscopy. *J. Nucl. Mater.* **2015**, *462*, 296–303. [CrossRef]
63. Frost, R.L.; Cejka, J.; Weier, M.L.; Martens, W. Molecular structure of the uranyl silicates—A Raman spectroscopic study. *J. Raman Spectrosc.* **2006**, *37*, 538–551. [CrossRef]
64. Alexander, E.B.; Coleman, R.G.; Keeler-Wolfe, T.; Harrison, S.P. *Serpentine Geoecology of Western North America: Geology, Soils and Vegetation*; Oxford University Press: Oxford, UK, 2007.
65. Frost, B.R.; Beard, J. On silica activity and serpentinization. *J. Petrol.* **2007**, *48*, 1351–1368. [CrossRef]
66. Fyfe, W.S. Heats of chemical reactions and submarine heat production. *Geophys. J. Roy. Astron. Soc.* **1974**, *37*, 213–215. [CrossRef]
67. Monin, C.; Chavagnac, V.; Boulart, C.; Ménez, B.; Gérard, M.; Gérard, E.; Quemeneur, M.; Erauso, G.; Postec, A.; Guentas-Dombrowski, L.; et al. The low temperature hyperalkaline hydrothermal system of the Prony Bay (New Caledonia). *Biogeosci. Discuss.* **2014**, *11*, 6221–6267.
68. Ulrich, M.; Picard, C.; Guillot, S.; Chauvel, C.; Cluzel, D.; Meffre, S. Multiple melting stages and refertilization as indicators for ridge to subduction formation: The New Caledonia ophiolite. *Lithos* **2010**, *115*, 223–236. [CrossRef]
69. Chamberlain, J.A.; McLeod, C.R.; Traill, R.J.; Lachance, G.R. Native metals in the Muskox Intrusion. *Can. J. Earth Sci.* **1965**, *2*, 188–215. [CrossRef]
70. Yamamoto, S.; Komiya, T.; Hirose, K.; Maruyama, S. Coesite and clinopyroxene exsolution lamellae in chromitites: In-situ ultrahigh-pressure evidence from podiform chromitites in the Luobusa ophiolite, southern Tibet. *Lithos* **2009**, *109*, 314–322. [CrossRef]
71. Cartigny, P. Stable Isotopes and the Origin of Diamond. *Elements* **2005**, *1*, 79–84. [CrossRef]
72. Bouilhol, P.; Debret, B.; Inglis, E.C.; Warembourg, M.; Grocolas, T.; Rigaudier, T.; Villeneuve, J.; Burton, K.W. Decoupling of inorganic and organic carbon during slab mantle devolatilisation. *Nature. Comm.* **2022**, *13*, 308. [CrossRef]
73. McCollom, T.M.; Bach, W. Thermodynamic constraints on hydrogen generation during serpentinization of ultramafic rocks. *Geochim. Cosmochim. Acta* **2009**, *73*, 856–875. [CrossRef]
74. Stagno, V.; Frost, D.J. Carbon speciation in the asthenosphere: Experimental measurements of the redox conditions at which carbonate-bearing melts coexist with graphite or diamond in peridotite assemblages. *Earth Planet. Sci. Lett.* **2010**, *300*, 72–84. [CrossRef]
75. Bundy, T.P.; Kasper, J.S. Hexagonal Diamond-A New Form of Carbon. *Chem. Phys.* **1967**, *46*, 3437–3446. [CrossRef]
76. Daulton, T.L.; Amari, S.; Scott, A.C.; Hardiman, M.; Pinter, N.; Anderson, R.S. Comprehensive Analysis of Nanodiamond Evidence Relating to the Younger Drays Impact Hypothesis. *J. Quat. Sci.* **2017**, *32*, 7–34. [CrossRef]
77. Cayron, C.; Hertog, M.D.; Latu-Romain, L.; Mouchet, C.; Secouard, C.; Rouviere, J.-L.; Rouviere, E.; Simonato, J.-P. Odd electron diffraction patterns in silicon nanowires and silicon thin films explained by microtwins and nanotwins. *J. Appl. Cryst.* **2008**, *42*, 242–252. [CrossRef] [PubMed]
78. Moore, R.O.; Gurney, J.J. *Proceedings of the Fourth International Kimberlite Conference, Kimberlites and Related Rocks*; Their Mantle/Crust Setting, Diamonds and Diamond Exploration; Geological Society of Australia Special Publication 14; Blackwell Scientic: Cambridge, UK, 1989; pp. 1029–1041.
79. Mudd, G.M. *Compilation of Uranium Production History and Uranium Deposit Data Across Australia*; SEA-US Inc.: Melbourne, Australia, 2006; pp. 1–46.
80. Finch, R.; Ewing, R. The corrosion of uraninite under oxidizing conditions. *J. Nucl. Mater.* **1992**, *190*, 133–156. [CrossRef]
81. Pérez, I.; Casas, I.; Martín, M.; Bruno, J. The thermodynamics and kinetics of uranophane dissolution in bicarbonate test solutions. *Geochim. Cosmochim. Acta* **2000**, *64*, 603–608. [CrossRef]
82. Shvareva, T.Y.; Mazeina, L.; Gorman-Lewis, D.; Burns, P.C.; Szymanowski, J.E.; Fein, J.B.; Navrotsky, A. Thermodynamic characterization of boltwoodite and uranophane: Enthalpy of formation and aqueous solubility. *Geochim. Cosmochim. Acta* **2011**, *75*, 5269–5282. [CrossRef]

83. Skinner, H.C.W.; Jahren, A.H. Biomineralization. In *Treatise on Geochemistry*; Holland, H.D., Turekian, K.K., Eds.; Elsevier: Amsterdam, The Netherlands, 2003; Volume 8, pp. 1–69.
84. Ayers, J.C.; Watson, E.B. Solubility of Apatite, Monazite, Zircon, and Rutile in Supercritical Aqueous Fluids with Implications for Subduction Zone Geochemistry. *Philos. Trans. Phys. Sci. Eng.* **1991**, *335*, 365–375.